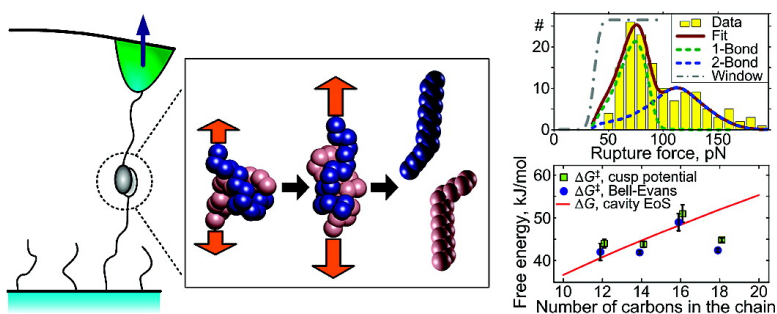**Article**

Pairwise Interactions between Linear Alkanes in Water Measured by AFM Force Spectroscopy

Chad Ray, Jason R. Brown, Andrea Kirkpatrick, and Boris B. Akhremitchev

More About This Article

Additional resources and features associated with this article are available within the HTML version:

- Supporting Information
- Links to the 1 articles that cite this article, as of the time of this article download
- Access to high resolution figures
- Links to articles and content related to this article
- Copyright permission to reproduce figures and/or text from this article

View the Full Text HTML

Pairwise Interactions between Linear Alkanes in Water Measured by AFM Force Spectroscopy

Chad Ray, Jason R. Brown, Andrea Kirkpatrick,[†] and Boris B. Akhremitchev*

Department of Chemistry, Duke University, Durham, North Carolina 27708

Received March 2, 2008; E-mail: boris.a@duke.edu

Abstract: Pairwise interactions between *n*-alkanes from decane to octadecane in water have been studied by single-molecule force spectroscopy. The interacting molecules are covalently tethered to the glass substrate and to the probe of an atomic force microscope by water-soluble linkers to facilitate single-molecule detection. However, the measured distribution of rupture forces deviates significantly from the distribution predicted by theoretical models for rupture of individual bonds. To describe the statistics of rupture forces, an analytical model that considers near-simultaneous rupture of two bonds loaded by tethers with different lengths is introduced. The common most probable force analysis approach is used for comparison. In both data analyses, the possible systematic errors due to nonlinear elasticity of polymeric tethers and variations in the shape of the potential of mean force were considered. Experimental distributions of rupture forces are well-fit by the two-bond rupture model using a single set of kinetic parameters for different experiments, while the most probable force approach yields parameters that vary significantly for different samples. The measured activation energies for dissociation of alkanes are close to the free energies predicted by cavity models of hydrophobic interactions. The surface free-energy density is estimated to be ~ 21 kJ/(mol nm^2) and is close to the upper limit of free energies used in the computer simulations of hydrophobic interactions in proteins. In contrast to the predictions of the cavity models, the measured activation energy does not increase monotonically with increase in alkane chain size. To explain this discrepancy and the measured distance to the transition-state barrier (~ 0.6 nm), it is suggested that alkanes undergo conformational transition to the collapsed state upon dimerization. Change in the alkane conformation from extended to helical has been observed previously for binding of alkanes in water to hydrophobic synthetic receptors. Here, however, conformational change is suggested without geometrical constraints imposed by small cavitands. The proposed collapsed state of the alkane dimers has implications for the kinetics of self-assembly of surfactant micelles.

1. Introduction

Hydrophobic interactions are among the most dominant forces between biological molecules in aqueous environment[1] governing native protein folding,[2,3] self-assembly of lipid bilayers,[4] and pathological supramolecular aggregation.[5] Hydrophobic interactions result from the strong attraction between water molecules and the weak attraction between water and nonpolar solutes, yielding net cohesive forces between the nonpolar solutes.[6–8] Hydrophobic attraction depends on the size and geometry of associating nonpolar solutes.[9–14] Theories predict that the nature of hydrophobicity changes from entropy-driven to enthalpic at the biologically important solute size scale of approximately 1 nm.[12,15] Hydrophobic interactions are difficult to

study experimentally in the pure form (in the absence of surfactants) at the 1-nm size scale because of the low solubility of hydrophobic compounds[13,16,17] and limitations of the measurement techniques.[18,19] Theoretical models and computer simulations of pairwise interactions between hydrophobic species in water predict that for sufficiently large solutes a depletion of water density between the solutes might occur (dewetting).[9,12,15,20–23] Direct measurements using hydrophobic surfaces[24–26] have been limited to length scales significantly exceeding 1 nm, and previous experimental results

---

† Current address: Division of Chemistry and Chemical Engineering, California Institute of Technology, Pasadena, CA 91125.

(1) Leckband, D.; Israelachvili, J. *Q. Rev. Biophys.* **2001**, *34*, 105–267.
(2) Kauzmann, W. *Adv. Protein Chem.* **1959**, *14*, 1–63.
(3) Dill, K. A. *Biochemistry* **1990**, *29*, 7133–7155.
(4) Tanford, C. *Science* **1978**, *200*, 1012–1018.
(5) Dobson, C. M. *Philos. Trans. R. Soc. London, Ser. B* **2001**, *356*, 133–145.
(6) Nemethy, G.; Scheraga, H. A. *J. Phys. Chem.* **1962**, *66*, 1773–1789.
(7) Tanford, C. *The Hydrophobic Effect: Formation of Micelles and Biological Membranes*; Wiley: New York, 1973.
(8) Blokzijl, W.; Engberts, J. *Angew. Chem., Int. Ed.* **1993**, *32*, 1545–1579.

(9) Wallqvist, A.; Berne, B. J. *J. Phys. Chem.* **1995**, *99*, 2893–2899.
(10) Garde, S.; Hummer, G.; Paulaitis, M. E. *Faraday Discuss.* **1996**, 125–139.
(11) Gallicchio, E.; Kubo, M. M.; Levy, R. M. *J. Phys. Chem. B* **2000**, *104*, 6271–6285.
(12) Chandler, D. *Nature* **2005**, *437*, 640–647.
(13) Ashbaugh, H. S.; Pratt, L. R. *Rev. Mod. Phys.* **2006**, *78*, 159–178.
(14) Sobolewski, E.; Makowski, M.; Czaplewski, C.; Liwo, A.; Oldziej, S.; Scheraga, H. A. *J. Phys. Chem. B* **2007**, *111*, 10765–10774.
(15) Huang, X.; Margulis, C. J.; Berne, B. J. *J. Phys. Chem. B* **2003**, *107*, 11742–11748.
(16) Plyasunov, A. V.; Shock, E. L. *Geochim. Cosmochim. Acta* **2000**, *64*, 439–468.
(17) Maczynski, A.; Wisniewska-Goclowska, B.; Goral, M. *J. Phys. Chem. Ref. Data* **2004**, *33*, 549–577.
(18) Skvarla, J. *Adv. Colloid Interface Sci.* **2001**, *91*, 335–390.
(19) Meyer, E. E.; Rosenberg, K. J.; Israelachvili, J. *Proc. Natl. Acad. Sci. U.S.A.* **2006**, *103*, 15739–15746.

indicating a decrease in water density with the formation of nanobubbles are still debated.[27–29]

Recently, a single-molecule force spectroscopy[30] technique was developed to quantify interactions between individual hydrophobic molecules,[31–33] investigate the solvent-dependent unraveling of polystyrene in aqueous environment,[34] and study the contribution of hydrophobic collapse to the folding of extended protein molecules.[35] In dynamic force spectroscopy experiments that investigate dissociation between individual molecules, the molecular bond is subjected to an external load and the rupture force is measured as a function of the loading rate. Statistical data analysis of rupture forces and the apparent loading rates quantifies the distance between the equilibrium and the transition states ($x^{\ddagger}$, henceforth called *barrier width* for brevity) and the dissociation rate at no force k_0 for the force-driven reaction in the direction of a pulling coordinate. These kinetic parameters are often obtained by applying the Bell–Evans empirical model to the data and extrapolating the measurements to zero-applied force.[30,36–40] Assumptions in the model, (1) linear elasticity (harmonicity) of the polymeric tethers that are employed for pulling on the molecules and (2) the triangular shape of the potential of mean force (pmf), might result in substantial systematic errors in the kinetic parameters.[33,41–45] Improvements in data analysis have addressed these assumptions,[33,45] as briefly described below. However, the improved data analysis approach is not sufficient to reproduce the probability distribution of rupture forces measured experimentally. Histograms of measured rupture forces often contain a high force shoulder or tail that might affect the kinetic

parameters.[45,46] In this study, we use a model that assumes that the high rupture forces correspond to the rupture between two pairs of molecules with the same kinetic parameters for each pair but tethered by linkers of different length. This new extended model explains the large width of the distribution of rupture forces and eliminates the influence of the high rupture forces on kinetic parameters. We apply this new data analysis methodology to an investigation of the solute size dependence of the kinetic parameters of pairwise dissociation between alkanes in water.

In our experiments, alkane molecules of different sizes are covalently tethered via hydrophilic poly(ethylene glycol) (PEG) linkers to the glass substrate and to the probe of an atomic force microscope (AFM). This double-tether approach facilitates single-molecule measurements and removes spurious surface effects.[31,32,47] Studied alkanes include decane, dodecane, tetradecane, hexadecane, and octadecane. Only symmetric pairs (e.g., dodecane–dodecane) have been studied. The two-bond model is used to fit the rate-dependent distributions of rupture forces and extract kinetic parameters corrected for the identified systematic errors. The resulting kinetic parameters provide new molecular-level insights about the pairwise hydrophobic interactions between alkanes in water.

2. Theoretical Models

2.1. Theoretical Model for the Most Probable Rupture Forces. The probability density of the bond rupture p as a function of loading force F can be calculated according to:[30,48]

$$p(F) = -\frac{ds(F)}{dF} = \frac{k(F)}{v_F(F)} \cdot s(F) = \frac{k(F)}{v_F(F)} \cdot \exp\left[-\int_0^F \frac{k(F')}{v_F(F')}\,dF'\right] \quad (1)$$

Here $s(F)$ is the bond survival probability, $k(F)$ is the force-dependent dissociation rate, and $v_F(F)$ is the loading rate $v_F = dF/dt$. The dissociation rate k dependence on force can be described by different models of intermolecular potentials,[43,49–53] and the loading rate depends on the pulling velocity, spring constant of the force sensor, and tether dynamics.[37,41,42] In several special cases, eq 1 can be integrated to obtain an analytical formula.[38,45,49–51] Numerical integration can be easily performed to extract the kinetic parameters by fitting a model that describes the force dependence of dissociation rate to the experimental data without using analytical approximations.

The most probable force F^* can be determined from $dp(F)/dF = 0$, and the resulting equation for F^* is:

$$k(F^*)^2 + v_F{}'(F^*) \cdot k(F^*) = v_F(F^*) \cdot k'(F^*) \quad (2)$$

The prime in this and in the following equations means differentiation with respect to force. In constant velocity mode of force spectroscopy experiments, the force sensor with the spring constant k_c moves at a constant velocity v. When the

(20) Lum, K.; Luzar, A. *Phys. Rev. E* **1997**, *56*, R6283–R6286.
(21) Widom, B.; Bhimalapuram, P.; Koga, K. *Phys. Chem. Chem. Phys.* **2003**, *5*, 3085–3093.
(22) Rajamani, S.; Truskett, T. M.; Garde, S. *Proc. Natl. Acad. Sci. U.S.A.* **2005**, *102*, 9475–9480.
(23) Choudhury, N.; Pettitt, B. M. *J. Am. Chem. Soc.* **2005**, *127*, 3556–3567.
(24) Christenson, H. K.; Claesson, P. M. *Adv. Colloid Interface Sci.* **2001**, *91*, 391–436.
(25) Doshi, D. A.; Watkins, E. B.; Israelachvili, J. N.; Majewski, J. *Proc. Natl. Acad. Sci. U.S.A.* **2005**, *102*, 9458–9462.
(26) Fa, K. Q.; Nguyen, A. V.; Miller, J. D. *J. Phys. Chem. B* **2005**, *109*, 13112–13118.
(27) Ashbaugh, H. S.; Pratt, L. R.; Paulaitis, M. E.; Clohecy, J.; Beck, T. L. *J. Am. Chem. Soc.* **2005**, *127*, 2808–2809.
(28) Ball, P. *Nature* **2003**, *423*, 25–26.
(29) Yaminsky, V.; Ohnishi, S. *Langmuir* **2003**, *19*, 1970–1976.
(30) Evans, E.; Ritchie, K. *Biophys. J.* **1997**, *72*, 1541–1555.
(31) Ray, C.; Akhremitchev, B. B. *J. Am. Chem. Soc.* **2005**, *127*, 14739–14744.
(32) Ray, C.; Brown, J. R.; Akhremitchev, B. B. *J. Phys. Chem. B* **2006**, *110*, 17578–17583.
(33) Gu, C.; Ray, C.; Guo, S.; Akhremitchev, B. B. **2007**, *111*, 12898–12905.
(34) Gunari, N.; Balazs, A. C.; Walker, G. C. *J. Am. Chem. Soc.* **2007**, *129*, 10046–10047.
(35) Walther, K. A.; Grater, F.; Dougan, L.; Badilla, C. L.; Berne, B. J.; Fernandez, J. M. *Proc. Natl. Acad. Sci. U.S.A.* **2007**, *104*, 7916–7921.
(36) Bell, G. I. *Science* **1978**, *200*, 618–627.
(37) Rief, M.; Fernandez, J. M.; Gaub, H. E. *Phys. Rev. Lett.* **1998**, *81*, 4764–4767.
(38) Strunz, T.; Oroszlan, K.; Schumakovitch, I.; Guntherodt, H. J.; Hegner, M. *Biophys. J.* **2000**, *79*, 1206–1212.
(39) Neuert, G.; Albrecht, C.; Pamir, E.; Gaub, H. E. *FEBS Lett.* **2006**, *580*, 505–509.
(40) Merkel, R.; Nassoy, P.; Leung, A.; Ritchie, K.; Evans, E. *Nature* **1999**, *397*, 50–53.
(41) Evans, E.; Ritchie, K. *Biophys. J.* **1999**, *76*, 2439–2447.
(42) Friedsam, C.; Wehle, A. K.; Kuhner, F.; Gaub, H. E. *J. Phys.: Condens. Matter* **2003**, *15*, S1709–S1723.
(43) Dudko, O. K.; Hummer, G.; Szabo, A. *Phys. Rev. Lett.* **2006**, *96*, 108101.1108101.4.
(44) Schlierf, M.; Rief, M. *Biophys. J.* **2006**, *90*, L33–L35.
(45) Ray, C.; Brown, J. R.; Akhremitchev, B. B. *J. Phys. Chem. B* **2007**, *11*, 1963–1974.

(46) Ray, C.; Brown, J. R.; Akhremitchev, B. B. *Langmuir* **2007**, *23*, 6076–6083.
(47) Ratto, T. V.; Langry, K. C.; Rudd, R. E.; Balhorn, R. L.; Allen, M. J.; McElfresh, M. W. *Biophys. J.* **2004**, *86*, 2430–2437.
(48) Garg, A. *Phys. Rev. B* **1995**, *51*, 15592–15595.
(49) Dudko, O. K.; Filippov, A. E.; Klafter, J.; Urbakh, M. *Proc. Natl. Acad. Sci. U.S.A.* **2003**, *100*, 11378–11381.
(50) Hummer, G.; Szabo, A. *Biophys. J.* **2003**, *85*, 5–15.
(51) Hanke, F.; Kreuzer, H. J. *Phys. Rev. E* **2006**, *74*, 031909.1031909.5.
(52) Sheng, Y.-J.; Jiang, S. Y.; Tsao, H.-K. *J. Chem. Phys.* **2005**, *123*, 091102.
(53) Hyeon, C.; Thirumalai, D. *J. Phys.: Condens. Matter* **2007**, *19*, 113101.
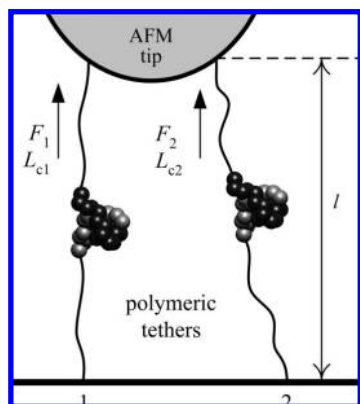
Figure 1. Model of rupture of two parallel bonds.

polymeric tether is pulling on the AFM tip and on the molecular bond with force F, the displacement z of the probe is given by $z = v \cdot t = F/k_c + l(F)$, where $l(F)$ is the force-dependent length of the tether. Therefore, $v_F(F) = [(k_c v)^{-1} + l'(F)/v]^{-1}$. Using the most probable loading rate v_F^* at the rupture (apparent loading rate[42]), eq 2 for the most probable force becomes[33]

$$k_c v_F^* \cdot k(F^*) \cdot l''(F^*) = [k_c l'(F^*) + 1] \cdot [k^2(F^*) - v_F^* \cdot k'(F^*)] \quad (3)$$

Equation 3 does not use any specific tether dynamic model and does not assume any particular dependence of the dissociation rate on loading force. It can be solved numerically for any selected tether dynamics and dissociation rate models to compute the most probable force F^* dependence on the most probable loading rate v_F^*. Assumption of harmonic tethers $l''(F) = 0$ simplifies eq 3 to $k^2(F^*) = v_F^* \cdot k'(F^*)$. However, this assumption might result in noticeable systematic error in the kinetic parameters,[45] and it is not used in our data processing.

2.2. Multiple Tip–Surface Bonds. With sufficiently high loading rate, eq 1 predicts that the probability of rupture rapidly increases with an increase of force after the rupture force exceeds the most probable force F^*. However, in many force spectroscopy experiments, including our measurements of interactions between alkane molecules,[45] histograms of rupture forces contain a high force tail that cannot be described by eq 1 using single values of the kinetic parameters.[54] It can be suggested that these high forces come from the simultaneous rupture of more than one molecular bond.[55,56] An approximate analytical model for the rupture of two parallel bonds that are pulled by the tethers of different length is described below.

The rupture of two parallel bonds is schematically illustrated in Figure 1. In this figure, the interacting molecules are represented by irregularly shaped beads and the polymeric tethers by wavy lines. The force applied by the cantilever force sensor is distributed between the two bonds. Upon rupture of one molecular bond, a part of the applied force that remains after a partial cantilever relaxation is applied to the second bond. The second bond might rupture nearly instantaneously on the time scale of force spectroscopy measurements. Therefore, such double-rupture events will

be detected as a single rupture. If both bonds do not rupture during the same rupture event, the second independent rupture will be detected in the force plot. Since either of the two bonds might rupture first, the survival probability of two bonds remaining intact equals the product of two survival probabilities:

$$S(F_\Sigma) = S_1(F_\Sigma) \cdot S_2(F_\Sigma) \quad (4)$$

Here, $F_\Sigma = F_1 + F_2$ is the sum of forces along individual bonds, and S is the bond survival probability; the subscripts indicate ruptures of individual bonds. The probability density (PD) function $P(F)$ can be calculated according to eqs 1 and 4 as:

$$P(F_\Sigma) = -\frac{dS(F_\Sigma)}{dF_\Sigma} = S_1(F_\Sigma) \cdot P_2(F_\Sigma) + S_2(F_\Sigma) \cdot P_1(F_\Sigma) \quad (5)$$

In AFM experiments in which the probe moves at constant velocity v, the survival probability of a single bond will differ from the survival probability of the identical bond when two bonds are parallel because of the different dynamics of loading. However, numerical estimates show that this difference is small, and it will not be considered below. Therefore, the PD becomes:

$$P(F_\Sigma) = s(F_1) \cdot p(F_2) \cdot \frac{dF_2}{dF_\Sigma} + s(F_2) \cdot p(F_1) \cdot \frac{dF_1}{dF_\Sigma} \quad (6)$$

Here, F_1 and F_2 are the forces along the shorter and the longer tethers, and the small letters for probability density and survival probability denote the force functions of two identical bonds. Using the high force asymptotic expression of the freely jointed chain (aFJC) model (applicable here because of the relatively high rupture forces measured by AFM),[45] we can relate the forces along individual tethers to the total force $F_\Sigma = F_1 + F_2$ according to:

$$F_1 = \frac{1}{2\delta L_c}\Big[F_\Sigma \delta L_c - F_K(2 + \delta L_c) + \sqrt{4F_K F_\Sigma \delta L_c + [F_\Sigma \delta L_c - F_K(2 + \delta L_c)]^2}\Big] \quad (7)$$
$$F_2 = F_\Sigma - F_1$$

Here, δL_c is the relative difference in the length between the longer and the shorter tethers $\delta L_c = (L_{c2} - L_{c1})/L_{c1}$, and F_K is the characteristic thermal Kuhn force $F_K = k_B T/l_K$ where k_B is the Boltzmann's constant, T is the absolute temperature, and l_K is the Kuhn length.

In AFM measurements, molecules are picked at random, and consequently the relative difference between the tether lengths δL_c is not controlled in the experiments. Therefore, to obtain a PD to fit the experimental histograms, the distribution given by eq 6 should be averaged over the distribution of δL_c values:

$$\Pi(F_\Sigma) = \int_0^{\delta L_{max}} p_t(\delta L_c) \cdot P(F_\Sigma, \delta L_c)\, d\delta L_c \quad (8)$$

Here, $p_t(\delta L_c)$ is the probability density to encounter a particular value of δL_c, and δL_{max} is the maximum δL_c value at which the two ruptures are still detected as a single rupture event. For simplicity, we assume that $p_t(\delta L_c)$ is constant. Substituting eq 6 into eq 8, the averaged PD becomes

$$\Pi(F_\Sigma) = \frac{1}{\delta L_{max}} \int_0^{\delta L_{max}} [s(F_1) \cdot p(F_2) \cdot (dF_2/dF_\Sigma) + s(F_2) \cdot p(F_1) \cdot (dF_1/dF_\Sigma)]\, d\delta L_c$$
$$\approx \frac{1}{\delta L_{max}}\Big[s(F_1, \delta L_{max}/2)\int_0^{\delta L_{max}} p(F_2)\, d\delta L_c + s(F_2, \delta L_{max}/2)\int_0^{\delta L_{max}} p(F_1)\, d\delta L_c\Big] \quad (9)$$

(54) Raible, M.; Evstigneev, M.; Bartels, F. W.; Eckel, R.; Nguyen-Duong, M.; Merkel, R.; Ros, R.; Anselmetti, D.; Reimann, P. *Biophys. J.* **2006**, *90*, 3851–3864.

(55) Kudera, M.; Eschbaumer, C.; Gaub, H. E.; Schubert, U. S. *Adv. Funct. Mater.* **2003**, *13*, 615–620.

(56) Sulchek, T. A.; Friddle, R. W.; Langry, K.; Lau, E. Y.; Albrecht, H.; Ratto, T. V.; DeNardo, S. J.; Colvin, M. E.; Noy, A. *Proc. Natl. Acad. Sci. U.S.A.* **2005**, *102*, 16638–16643.

In the second equality in eq 9, the survival probabilities under the integral are approximated by a constant value computed in the middle of the integration interval. Another approximation is that derivatives of the forces along individual tethers with respect to the total force are approximated by one-half. Approximate integration of eq 9 using eq 7 gives

$$\Pi(F_\Sigma) \approx s(F_\Sigma/2) \cdot [s(F_2) - s(F_1)]/(F_1 - F_2) \qquad (10)$$

Here, forces F_1 and F_2 are calculated according to eq 7 by substituting δL_c with δL_{max}. Equation 10 is asymptotically accurate for small values of δL_c. In this limit, the right-hand side becomes $s(F_\Sigma/2) \cdot p(F_\Sigma/2)$ and equals to eq 6 when $F_1 = F_2 = F_\Sigma/2$. However, eq 10 is normalized only for small values of δL_c (<0.02) because in the derivation derivatives dF_1/dF_Σ and dF_2/dF_Σ are replaced with 1/2. This replacement is not accurate because for increasing δL_c the derivative dF_1/dF_Σ approaches 1 and the derivative dF_2/dF_Σ approaches 0. The consequence of this approximation is shown in Figure 2. The normalization is improved if eq 10 is multiplied by a constant factor:

$$\Pi(F_\Sigma) \approx (1 + 2\delta L_{max}) \cdot s(F_\Sigma/2) \cdot [s(F_2) - s(F_1)]/(F_1 - F_2) \qquad (11)$$

This modification preserves the asymptotic accuracy at small values of δL_c.

An assumption was made in deriving eq 11 that the distribution of the tether lengths is rectangular. However, according to mass spectrometry measurements this distribution is better approximated with a Gaussian curve. Therefore, the approximate eq 11 is compared to exact calculations according to eq 8 for rectangular and Gaussian distribution of the tether lengths.

For lengths of tethers l distributed according to Gaussian distribution with width σ_l centered at l_0 the probability density is

$$p_l(l) = \frac{1}{\sigma_l\sqrt{2\pi}} \exp\left[-\frac{(l - l_0)^2}{2\sigma_l^2}\right] \qquad (12)$$

The probability density to select two tethers with lengths different by δl is

$$p_d(\delta l) = \int_{-\infty}^{+\infty} p_l(l) \cdot p_l(l + \delta l) \, dl = \frac{1}{2\sigma_l\sqrt{\pi}} \exp\left[-\frac{\delta l^2}{4\sigma_l^2}\right] \qquad (13)$$
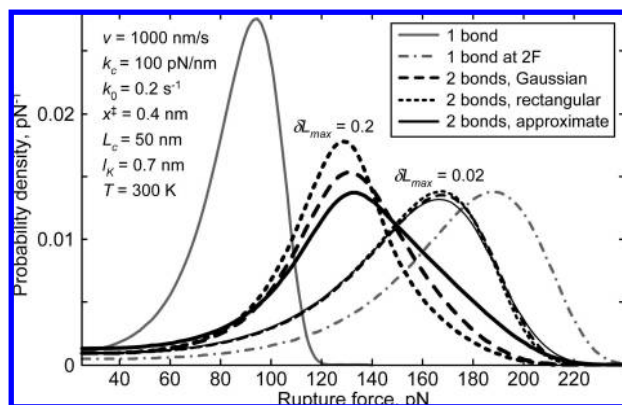

Figure 2. Comparison between exact and approximate probability density functions of a two-bond rupture. Exact models include the Gaussian and rectangular tether lengths distributions. Widths for rectangular distributions and approximate calculations by eq 11 are shown; widths for Gaussian distributions are lower by a factor of 2. Calculations use the Bell–Evans bond rupture model and FJC tether model. Other model parameters are shown.

Equation 13 shows that the Gaussian distribution of the difference in the tether lengths has a width that is a factor of $\sqrt{2}$ larger than the width of the distribution of the tether lengths. Therefore, the tether length distribution measured by mass spectrometry can be used to estimate the width of δL_c distribution. For the tethers used in this study, mass spectrometry measurements give a width of δL_c distribution of 0.2 (sample distributions of tether lengths have been shown previously).[31,33]

Figure 2 compares PDs calculated for Gaussian and rectangular distribution of δL_c by numerical integration of eq 8 (dashed and dotted lines) and approximate PDs calculated according to eq 11 (solid lines). Calculations use the Bell–Evans bond rupture model where $k(F) = k_0 \exp[F \cdot x^\ddagger/(k_B T)]$ and the FJC tether model where $l/L_c = \coth(F/F_K) - F_K/F$. As might be expected, the two-bond peaks are located between the single bond peak and the peak at the double rupture force. It can be noted that the approximate calculations reproduce the position of the maximum with reasonable accuracy; however, it gives more statistical weight to the distributions with lower δL_c values and consequently overestimates the rupture probability on the high force side of the peak. The approximate solution reproduces better the shape of the exact model that uses Gaussian distribution than the model that uses a rectangular distribution of tether lengths. Therefore, it might be expected that eq 11 will fit the high force tail in the experimentally measured histograms of rupture forces reasonably well.

It should be noted that the analytical model given by eq 11 predicts only the high rupture forces that are lower than twice the force of single interaction. In experiments, even higher rupture forces are sometimes observed.[55,57,58] It might be expected that the present model could be extended to higher forces than those considered here.

The histograms of the rupture forces include both single and the multiple bond rupture events. Therefore, the resulting distribution function to fit the experimental data is

$$P(F) = (1 - f_2)p(F) + f_2\Pi(F) \qquad (14)$$

where f_2 is the relative fraction of two-bond rupture events in the data. Including the two-bond rupture in the histogram fitting requires two additional parameters: the maximum relative difference in tether lengths δL_{max} and the fraction of two-bond events f_2. The first of these parameters determines the position of the high force peak, and the second parameter determines the amplitude of the two-bond ruptures.

3. Experimental Details

3.1. Sample Preparation. Samples were prepared similarly to the previously reported method.[31,32] All chemicals were purchased from Aldrich, unless specified. Only glass or Teflon reaction vessels were used for the sample preparation reactions. Briefly, cleaned silicon nitride AFM probes (Veeco, NP series probes) and glass coverslips (Fisher Scientific) were aminated with ethanolamine in dry DMSO for 72 h.[59] α-*N*-Hydroxysuccinimide−ω-maleimide−poly(ethylene glycol) (NHS−PEG−MD) (Nektar Therapeutics) linkers with mass averaged molecular weight of 3535 Da were covalently attached to the surface through the NHS−amine reaction and to 1-alkane thiols through the reaction of the terminal

(57) Sulchek, T.; Friddle, R. W.; Noy, A. *Biophys. J.* **2006**, *90*, 4686–4691.
(58) Snyder, P. W.; Lee, G.; Marszalek, P. E.; Clark, R. L.; Toone, E. J. *Proc. Natl. Acad. Sci. U.S.A.* **2007**, *104*, 2579–2584.
(59) Hinterdorfer, P.; Gruber, H. J.; Kienberger, F.; Kada, G.; Riener, C.; Borken, C.; Schindler, H. *Colloids Surf., B* **2002**, *23*, 115–123.

thiol with the PEG's MD terminal.[60] Both of these reactions were carried out simultaneously for 24 h in anhydrous toluene with 5% pyridine (v/v). Control measurements with "empty" tethers employed samples that include grafted PEG tethers reacted with 2-mercaptoethanol instead of alkane thiols. A second reaction to the surface amines was then performed with α-*N*-hydroxysuccinimide−ω-ethyl ether−poly(ethylene glycol) (SS−PEG) (Polysciences, Inc.) with a molecular weight of ∼1900 Da. This reaction backfilled the remaining surface area next to the longer PEG tethers[61] to hinder tethered alkanes from adsorption onto the solid substrate.[31,32] This reaction was performed for 48 h in toluene with 10% pyridine. A final reaction with acetic anhydride was performed overnight to block any remaining amines. The samples were then cleaned in water, toluene, DMF, and ethanol to remove physisorbed molecules and used immediately after preparation. All grafting reactions were conducted in anhydrous toluene to avoid aggregation of alkanes during sample preparation. Measurements were performed with the two combinations of substrates and AFM probes: both surfaces containing tethered alkanes, and the control set with one surface containing tethered alkanes and another containing ethoxy-capped PEG tethers.

3.2. Data Collection. Force spectroscopy measurements were performed with Asylum Research MFP-3D AFM using chemically modified silicon nitride probes (Veeco) with spring constants (in newtons/meter) for sets A and B, respectively, of decane: 0.055, 0.15; dodecane: 0.22, 0.06; tetradecane: 0.09, 0.05; hexadecane: 0.065, 0.06; and octadecane: 0.09, 0.18. Spring constants were found using the built-in thermal noise analysis method. Each cantilever was used for an entire set of probe velocities because the experimental determination of the spring constant might have ∼20% error.[62] The experimental procedure and the data processing were described previously.[31,32] Experiments were conducted in 0.05 M pH 7 phosphate buffer at 30 °C. A custom-made temperature stage was used to set the temperature and a custom-made O-ring was used to reduce evaporation of the phosphate buffer when the AFM probe was engaged over the sample. At least 4096 force curves were collected at a particular probe velocity in a series of measurements performed with different probe velocities ranging from 200 to 6000 nm/s. The interaction between tethered molecules was initiated by bringing two surfaces together. Formation of molecular bonds was facilitated by maintaining the tip−sample contact for 1 s. Rupture forces were detected during the reverse motion of the probe. Probe position was raster scanned over the sample's surface after each force plot measurement to obtain a good statistical average. Force−distance curves collected at each probe position were digitally stored for the subsequent analysis. Data processing and analysis was performed with custom-written software for Matlab.

3.3. Data Analysis. To distinguish rupture events between the tethered molecules from the ruptures between the tethered molecule and the substrate surface, the double tether approach was used.[31,32,47,56] Force−distance curves reveal that the rupture events occur at different probe positions above the sample surface. Before the rupture events, the polymer tethers were stretched with end-to-end distances far exceeding the average distances found at thermal equilibrium. This stretching results in a characteristic force-separation dependence that was used as an initial selection criterion in the data analysis. Long tethers were used to clearly identify rupture events between tethered molecules and to reduce effect of mechanical noise.[63] Rupture events that correspond to the sum of the tethers' stretched lengths were used in the statistical analysis of rupture forces. The range of contour lengths used in the analysis

includes the polydispersity of tethers as well as conformational transition of PEG tethers under force.[64] An extended freely jointed chain (eFJC) model that includes a conformational transition of PEG linkers[64] was fit to the last detected tether-stretching event, providing the contour lengths, the Kuhn lengths, and loading rate for each pulling event.[31,32] These values were used to account for the effects of the tether dynamics. The rupture forces and apparent loading rates measured at different probe velocities were binned into histograms with equal bin widths for further analysis.

3.4. Fit to Force vs Loading Rate Dependence. The most probable rupture forces were obtained from the histograms of rupture forces at different values of probe velocity. Histograms of rupture forces were fit with Gaussian curves multiplied by a window function to account for the limited force sensitivity.[31,32,42] The position and width of the window function were fit to the edge of the lowest retract velocity force histogram and adjusted based on the change in noise level for each probe velocity. Gaussian curves were selected for fitting these histograms because experimental data include a tail of higher forces (Figure 5) that are not present in the theoretical distributions of single interactions. The most probable force vs loading rate dependencies were then fit by eq 3. Two models were used for the dissociation rate dependence on force: the Bell−Evans model that corresponds to a triangular-shaped potential and the cusp potential model.[43] These models have been shown previously to yield the lowest and highest values of fitted kinetic parameters among other analytical models.[33,65] The cusp potential model explicitly uses the activation energy $\Delta G^{\ddagger}$.[43] This energy was included in the model as $\Delta G^{\ddagger} = k_{B}T \log (A/k_{0})$ where A is the Arrhenius prefactor. The prefactor A was kept at 10^{7} s^{-1} as was done previously.[32,45,46] Variations in the kinetic parameters due to uncertainty in the prefactor are discussed below.

3.5. Direct Histogram Fit to Force Probability Distribution. To account for the high force tail, the collected force histograms for each alkane were simultaneously fit to the two-bond rupture model. The fit parameters included the barrier width $x^{\ddagger}$, the zero-force dissociation rate k_{0}, the amplitude of the high force tail f_{2}, and the maximum relative difference in the length of tethers δL_{max}. For each alkane, the same values of $x^{\ddagger}$, k_{0}, and δL_{max} were used to fit different histograms collected with different probe velocities and different AFM probe sample pairs. The amplitude f_{2} was fit individually for each histogram to account for the variation in the probability of the two-bond rupture events. As above, limited force sensitivity was accounted for with a window function. The position of the window function was set to six standard deviations above the average rms noise of the force curves, and the width of the rising edge of the window was held at one rms noise value. The histograms were fit directly with eq 14. The single-bond survival probabilities and the PDs were calculated by numerical integration using the guessed values of the fit parameters. The fitting minimized the average rms fit error by using the Nelder−Mead direct search method included in the Matlab software. The tether and the dissociation rate models were the same as that in the force vs loading rate analysis described above.

In addition to including the high forces in the distribution, this fitting procedure accounted for the effects of tether stiffening by incorporating the eFJC polymer stretching model. Effects of the pmf shape were considered as well by using the cusp potential model in place of the Bell−Evans model.

4. Results

4.1. Force-Separation Plots. Figure 3 shows typical force-separation plots exhibiting molecular bond rupture events. The ruptures occurred at distances from the surface approximately corresponding to twice the length of the PEG tethers used in

(60) Hermanson, G. T. *Bioconjugate Techniques*; Academic Press: San Diego, CA, 1996.

(61) Huang, H. Q.; Cammers, A.; Penn, L. S. *Macromolecules* **2006**, *39*, 7064−7070.

(62) Proksch, R.; Schaffer, T. E.; Cleveland, J. P.; Callahan, R. C.; Viani, M. B. *Nanotechnology* **2004**, *15*, 1344−1350.

(63) Kuhner, F.; Gaub, H. E. *Polymer* **2006**, *47*, 2555−2563.

(64) Oesterhelt, F.; Rief, M.; Gaub, H. E. *New J. Phys.* **1999**, *1*, 6.

(65) Hukkanen, E. J.; Wieland, J. A.; Gewirth, A.; Leckband, D. E.; Braatz, R. D. *Biophys. J.* **2005**, *89*, 3434−3445.
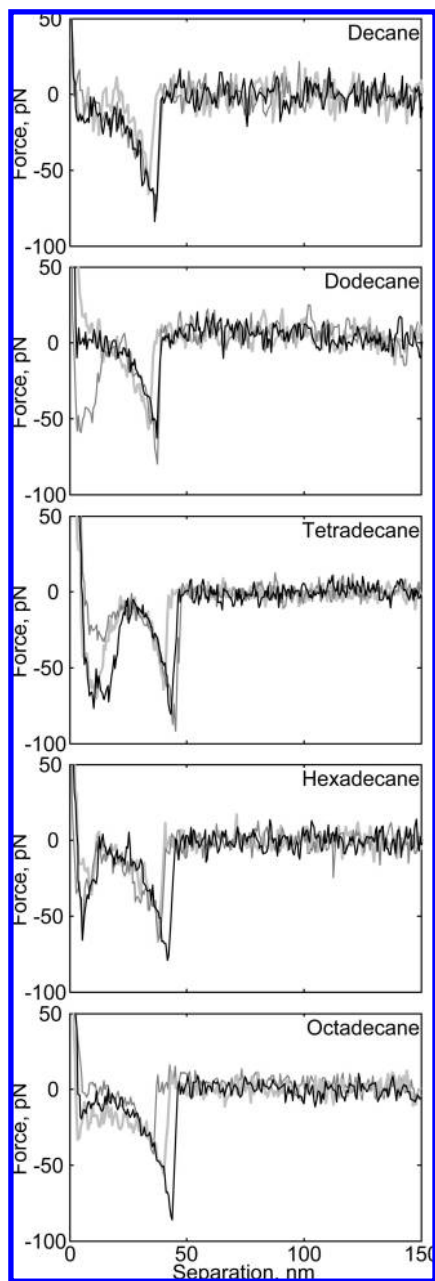
Figure 3. Representative force curves with double-tether rupture events for each of the alkanes tested.

the covalent surface modification. Characteristic polymer tether stretching events preceded each rupture event. Rupture events that have the tether contour length of less than 30 nm might correspond to events other than the desired double tether rupture events and were filtered out. This type of analysis is similar in practice to the unfolding of protein domains,[66] as the contour length is used as a "signature" of the desired molecular bond rupture events. Some of the curves shown in Figure 3 have initial adhesion, but the polymer spacer mitigates this interference by moving the desired rupture event off the surface by ∼45 nm, twice the length of the polymer spacers. The consistent separation distance of the rupture event is a "signature" used to identify the desired molecular rupture events.
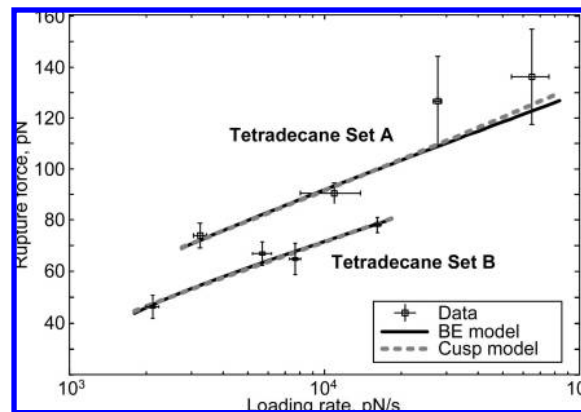
(66) Fisher, T. E.; Marszalek, P. E.; Fernandez, J. M. *Nat. Struct. Biol.* **2000**, *7*, 719–724.

Figure 4. Representatives of the most probable force vs most probable loading rate dependences fit with the Bell–Evans and cusp models.

Table 1. Data Fit with the Bell–Evans Model

sample/fit	$x^{\ddagger}$ (nm)	$\delta x^{\ddagger}$ (nm)	k_0 (1/s)	δk_0 (1/s)	$\Delta G^{\ddagger}$ (kJ/mol)	$\delta \Delta G^{\ddagger}$ (kJ/mol)
$C_{12}H_{25}$						
distribution fit	0.41	0.04	0.4	+0.5 −0.25	42	2
set A (F* vs v_F*)	0.22	0.06	3	4	38	3
set B (F* vs v_F*)	a	a	a	a	a	a
$C_{14}H_{29}$						
distribution fit	0.45	0.02	0.4	0.1	41.9	0.3
set A (F* vs v_F*)	0.27	0.06	1	3	40	5
set B (F* vs v_F*)	0.32	0.03	2.1	0.6	39.8	0.7
$C_{16}H_{33}$						
distribution fit	0.73	0.05	0.02	+0.03 −0.015	49	2
set A (F* vs v_F*)	0.6	0.1	0.01	0.08	50	19
set B (F* vs v_F*)	0.39	0.06	0.7	1.6	42	6
$C_{18}H_{37}$						
distribution fit	0.47	0.01	0.5	0.1	42.4	0.3
set A (F* vs v_F*)	0.33	0.06	1.9	2	39	3
set B (F* vs v_F*)	0.26	0.04	2	2	40	3

a Connotes too few data points for proper fitting.

To further demonstrate that the measured rupture events are between the molecules grafted at the ends of the polymer tethers, "empty tether" control experiments were performed. These experiments were performed exactly as the main experiments, except with a tip fully functionalized with the respective alkane-terminated polymer tethers and a sample with the ethoxy-capped polymer tethers. In these control experiments, the rupture events at the double-tether length are sometimes observed. However, a detection probability of such events is ∼0.05% of all surface approach–withdraw attempts. This probability is at least 5 times less and can be more than an order of magnitude less than the detection probability in the normal experiments (values are shown in Figure 6). This indicates that the majority of the measured double tether rupture events correspond to the forced unbinding of the tethered alkanes.

4.2. Fit to Force vs Loading Rate Dependence. Figure 4 shows the most probable force vs loading rate dependence as well as the corresponding fit lines (eq 3 was used in all fits) for two sets of tetradecane data (similar data sets and fits for all alkanes are included in the Supporting Information). The kinetic parameters from the fits are listed in Tables 1 and 2. The error bars in the graph correspond to the most probable rupture force and the loading rate errors that were determined from the Gaussian curve fits to the corresponding histograms. The fits for the Bell–Evans and cusp models are very close to each

Table 2. Data Fit with the Cusp Potential Model

sample/fit	$x^{\ddagger}$ (nm)	$\delta x^{\ddagger}$ (nm)	k_0 (1/s)	δk_0 (1/s)	$\Delta G^{\ddagger}$ (kJ/mol)	$\delta \Delta G^{\ddagger}$ (kJ/mol)
$C_{12}H_{25}$						
distribution fit	0.55	0.03	0.26	+0.13 −0.08	44	1
set A (F* vs v_F*)	0.28	0.26	1.5	0.8	39	1
set B (F* vs v_F*)	a	a	a	a	a	a
$C_{14}H_{29}$						
distribution fit	0.59	0.03	0.28	+0.09 −0.07	43.8	0.7
set A (F* vs v_F*)	0.33	0.08	1	2	41	6
set B (F* vs v_F*)	0.39	0.06	1.5	0.6	40	1
$C_{16}H_{33}$						
distribution fit	0.97	0.08	0.016	+0.019 −0.009	51	2
set A (F* vs v_F*)	0.9	0.2	0.001	0.01	58	50
set B (F* vs v_F*)	0.5	0.1	0.3	1	44	9
$C_{18}H_{37}$						
distribution fit	0.64	0.02	0.19	0.04	44.8	0.5
set A (F* vs v_F*)	0.40	0.08	1.4	1.7	40	3
set B (F* vs v_F*)	0.32	0.06	1	1.6	41	4

a Connotes too few data points for proper fitting.

other within each set of data. As noted previously,[33,65] here the barrier widths determined with the Bell−Evans model are systematically lower than the cusp model values, while the Bell−Evans dissociation rates are systematically higher and the activation free energies are correspondingly lower in comparison to the cusp model results. The offset between the two data sets is attributed to the higher probability of a two-bond encounter in set A.
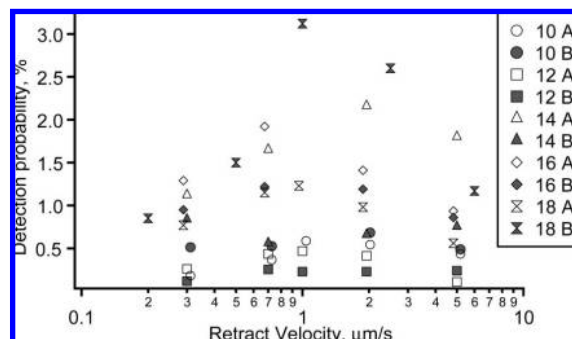

Figure 6. Detection probability for the collected sets of alkane data. Some points are slightly offset for clarity.

4.3. Direct Histogram Fit to Force Probability Distribution. The two-bond rupture model was used to simultaneously fit the histograms from two sets of data for each alkane sample (denoted set A and set B in order of collection) with the same kinetic parameters for both data sets. The spring constants varied between these sets because the data resulted from separately prepared tips and surfaces. Histograms for tetradecane are shown in Figure 5 (the histograms and fits for all alkanes are included in the Supporting Information).

Each histogram in Figure 5 represents data collected at a particular withdrawal speed (shown at the top of each histogram). The window function (dash-dotted line) and distribution fit for the new model eq 14 (gray solid line), with the single-bond (gray dotted line) and two-bond (black dotted line) components, are also shown in Figure 5. As with the most
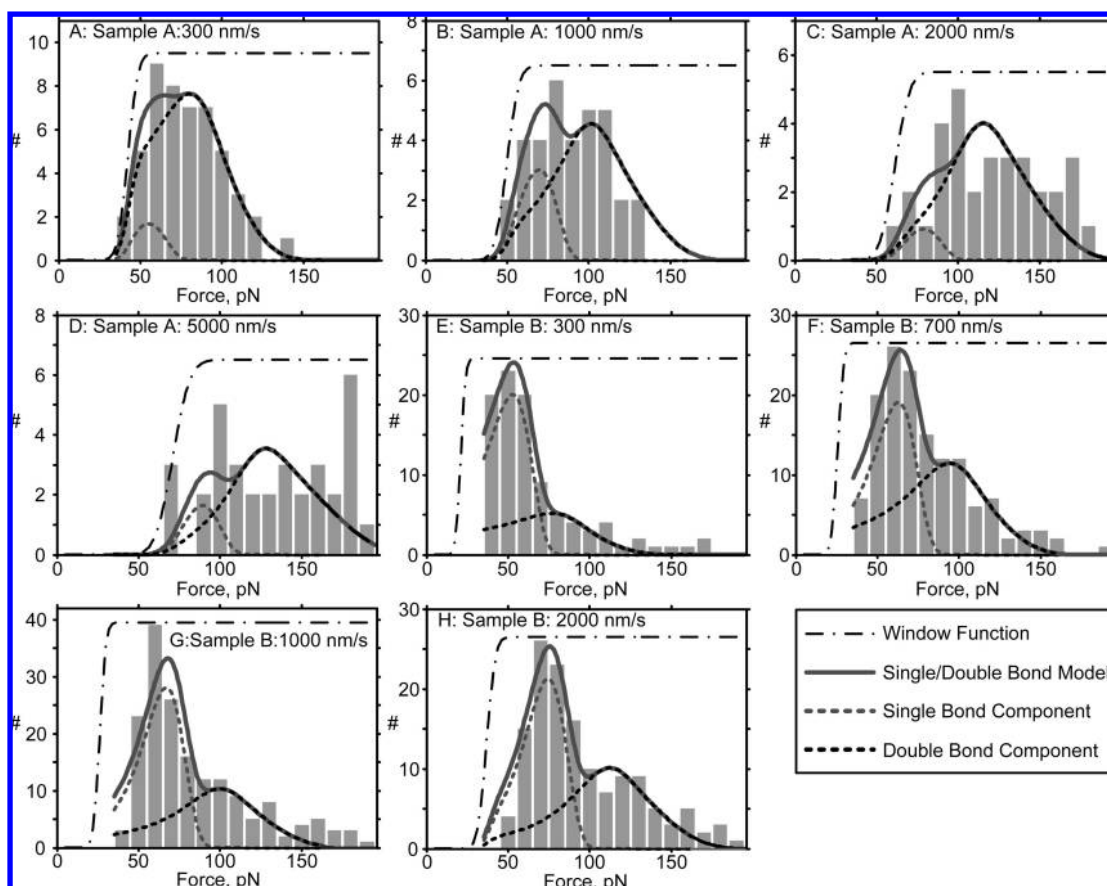

Figure 5. (A−H) Experimentally measured tetradecane rupture force histograms with the full distribution fits using the Bell−Evans kinetic model. (A−D) One set of collected data. (E−H) Second set of collected data. The model better fits the second set of data because there are more data points to fit.

probable force vs most probable loading rate fit, the fit lines for the Bell−Evans and cusp models are close to each other (data not shown), though the determined kinetic parameters differ. The trends in the determined kinetic parameters are the same as those for the linear fit method. Tables 1 and 2 show the kinetic parameters determined. Decane data was excluded from the tables because there were too few rupture events for a proper fitting. Note that the given errors in the kinetic parameters are similar to others in the field,[65] as well as our own previous work.[31,32,45,46]

4.4. Effect of the Prefactor on Activation Free Energy. In the Bell−Evans model, the barrier width $x^{\ddagger}$ and dissociation rate k_0 are independent of the Arrhenius prefactor. The estimated activation energy changes by ∼1.7 kJ/mol when the prefactor increases by a factor of 2. The prefactor of 10^7 s^{-1} used in our estimates is based on rate measurements of the cyclization of peptides of similar size to the alkane pairs used here.[67] According to theoretical models, the prefactor for the first contact between the chain end scales as N^{-2} where N is the number of monomers in the chain.[68,69] Therefore, in relation to the activation energy of hexadecane, this prefactor dependence changes the estimated activation energy for dodecane, tetradecane, and octadecane by 1.3, 0.6, and −0.6 kJ/mol, respectively. These offsets are close to the random errors of the measurements. Therefore, the activation energy values obtained with the same prefactor of 10^7 s^{-1} for different alkanes are discussed below.

4.5. Low Force Data Analysis Limit. Data were collected for linear alkane chains with chain lengths between 10 and 18 carbon atoms. Figure 6 shows that molecular rupture events are found rarely as the data is processed. Typically 1−2% of attempts show a molecular rupture event similar to events shown in Figure 3. The detection probability is much lower on average for decane and dodecane.

5. Discussion

5.1. Low Force Data Analysis Limit. The average detection probability is lowest for decane and dodecane (as seen in Figure 6 and the Supporting Information). Despite more than a dozen attempts, enough data for decane could not be collected for proper fitting, so it was excluded from the statistical analysis. Example force plots for decane are still included in Figure 3. The inherent noise in force in each force-separation plot makes low forces difficult to measure accurately and low force rupture events difficult to identify conclusively because they cannot be properly fit to polymer stretching models. This force barrier, represented in the analysis by the window function, obscures the low forces and makes useful experimental histograms difficult to obtain. While decane was below this barrier, dodecane yielded just enough events to put it above the edge of this barrier; though they have similar detection probabilities (as seen in the figure in the Supporting Information). One of the two sets of dodecane data had histograms with a sufficient number of rupture events for application of the most probable force vs most probable loading rate analysis. Both sets of dodecane data were used for the full fit procedure because it does not require histograms as populated as the most probable

force method for the analysis to be performed. Tetradecane, hexadecane, and octadecane data sets were sufficiently populated for both analyses. The low detection probability measured here (1−2% of approaches) is similar to the detection probability in a previous force spectroscopy study of interactions between hydrophobic fullerene C_{60} molecules.[33] This previous study, which used the same surface amination procedure as described here, indicated that surface attachment is sparse, and that the attached hydrophobic molecules do not form large aggregates on the surface as indicated by the low probability of rupture forces that are significantly above the forces predicted by the two-bond model (Figure 5 and figures shown in the Supporting Information, pages S11−S14).

5.2. Comparison of the Most Probable Force and Full Distribution Fitting. The most probable force vs loading rate analysis differed between samples (denoted as set A and set B) by as much as 50% in the barrier width and somewhat more in the dissociation rate between hexadecane samples, though the other sets were more consistent. The noted inconsistency between different sets is most likely caused by the uncertainty in the most probable force determination, and adds uncertainty to kinetic parameters obtained using common force spectroscopy data analysis approach. Because the high force tail widens and obscures the force distribution, the peak is much less resolved and correspondingly might be shifted to the higher forces and more difficult to accurately fit. The difference in the probability of the two-bond ruptures is a likely cause of the offset between two data sets of tetradecane data that are shown in Figure 4 as confirmed by the difference in the amplitude of the two-bond components shown in Figure 5. The variability of the potential of mean force for the dimer states of conformationally flexible alkanes might be suggested as an alternative explanation for the observed large width of the probability distribution.[54] This explanation is not used here because each data contains more than a hundred measurements of the rupture force obtained with different pairs of molecules. Therefore, it might be expected that the molecular bond heterogeneity should be the same for the data sets collected with different samples. However, the opposite is observed. The difference in the probability of the two-bond rupture between different samples can be attributed to the possible difference in the grafting density of alkanes, which is not controlled precisely during the sample preparation. This does not imply that there is no heterogeneity in molecular bond between alkanes in separately formed dimers, but only indicates that such heterogeneity, if present, affects the rupture forces less than the two-bond ruptures do.

The full distribution fitting method gave remarkably consistent kinetic parameters between all of the alkane samples. Because all of the data were used in the distribution fitting, small changes in some subset that may shift the peak do not significantly affect the fit parameters, as has been noted previously,[42,45,46] and is again confirmed here. The most probable force vs most probable loading rate analysis has a large uncertainty in the determined kinetic parameters (as noted above with the mismatch between set A and set B of each alkane measurement). Below, only kinetic parameters determined from full distribution fitting are considered to maximize the repeatability and comparability of these results.

5.3. High Force Tail. Previously the high force tail, as seen in Figure 8, was attributed to heterogeneity of molecular bonds[54] or to the nearly simultaneous rupture of two or more molecular bonds.[55,56] It is noted that the high force "tail" is minimized under conditions when the loading rate and binding state are more clearly

(67) Lapidus, L. J.; Eaton, W. A.; Hofrichter, J. *Proc. Natl. Acad. Sci. U.S.A.* **2000**, *97*, 7220–7225.
(68) Pastor, R. W.; Zwanzig, R.; Szabo, A. *J. Chem. Phys.* **1996**, *105*, 3878–3882.
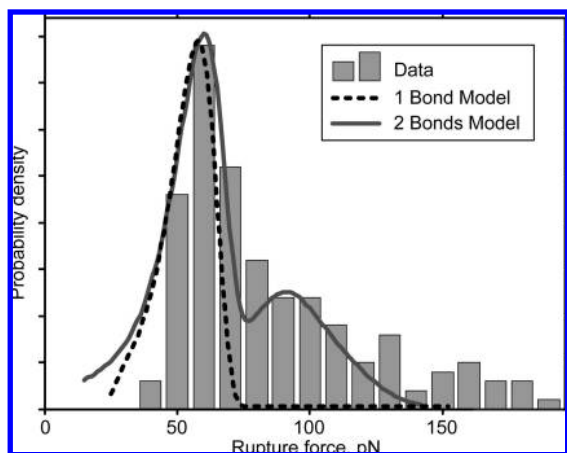(69) Chen, J. Z. Y.; Tsao, H. K.; Sheng, Y. J. *Phys. Rev. E* **2005**, *72*, 031804.

Figure 7. Comparison of the experimental histogram from Figure 5G to two calculated force probability densities, one for the standard single-bond model, and the other for the two-bond model.
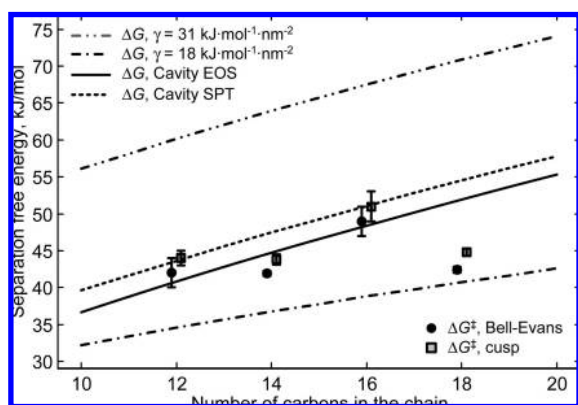

Figure 8. Measured transition-state free energies for each of the alkane chains in comparison with the thermodynamic free energy calculated with cavity models. Points are slightly offset for clarity.

defined, such as in protein unfolding experiments.[44,66,70–72] In protein unfolding experiments, the "signature" rupture of multiple protein domains is used to clearly distinguish the individual rupture events. The double tether method makes force spectroscopy broadly applicable to study pairwise interactions, but in comparison with the unfolding measurements has a diminished ability to identify the number of molecular bonds that are being dissociated in each rupture event.

Figure 7 compares an experimentally collected histogram of rupture forces with two calculated force probability densities. The calculations were based on the standard single-bond (black dashed line) and introduced two-bond (solid gray line) models. Both models were multiplied by the window function (which is not shown), similarly to the fitting. The parameters of the data represented in the histogram (contour and Kuhn lengths, δL_{max}, and f_2 amplitudes) were used with the kinetic parameters ($x^{\ddagger}$, k_0, and $\Delta G^{\ddagger}$) determined from fits by the two-bond model. Both calculations reproduce the main bond rupture peak, but the single bond model is unable to reproduce the high force tail.

As Figures 5 and 7 clearly demonstrate, the two-bond rupture model is adequate to explain the presence of the high force tail. However, it can be noted that the two-bond model does not fit the tail at very high rupture forces (above ∼130 pN in Figure 7). This failure is expected from the nature of the model. It might be suggested that these high forces come from the simultaneous ruptures of more than two bonds, and such events are not included in the model.

The fitting success and simplicity of the two-bond rupture model as an explanation of the deviation of the measured probability distribution from the individual bond model does not eliminate possible bond heterogeneity as a contributing factor to the high force tail. The effects of "hydrophobic" bond heterogeneity on the distribution of rupture forces can be determined from measurements that exclude the possibility of the multiple bond formation. Such measurements are not currently available.

5.4. Comparison with the Cavity Model. The activation energy $\Delta G^{\ddagger}$ obtained above is different from the thermodynamic free-energy difference between bound and dissociated states. However, according to theoretical calculations this difference is large for small (methane-like) solutes and decreases with an increase of the solute size.[23,73–75] Computer simulations of dimerization of neopentane in water[10,15] indicate that the difference between $\Delta G^{\ddagger}$ and ΔG is ∼10%; also, it is predicted that the activation barrier for the collapse of hydrophobic polymer is ∼10% of the unfolding barrier.[76] Therefore, it might be expected that the $\Delta G^{\ddagger}$ values measured here are close to the free-energy difference ΔG. Computer simulations of methane dimerization in water indicate that there is only small change in enthalpy upon contact of two molecules[77] and that the cavity contribution is the major part of that interaction.[11] Therefore, we compare the measured activation energies with the difference in the solvation free energy calculated from cavitation energies.[12,78] The solvation free-energy difference is calculated according to

$$\Delta G_d = 2 \cdot \Delta G_{cav}(R_{c,1}) - \Delta G_{cav}(R_{c,2}) \qquad (15)$$

Here, $\Delta G_{cav}(R_c)$ is the cavitation energy of a sphere with the cavity radius R_c, $R_{c,1}$ is the radius of the cavity that includes one molecule, and $R_{c,2}$ is the radius of the cavity that includes two molecules. Two cavity models are used below for the comparison: one uses the empirical cavity equation of state (cEOS)[32,79] and another is based on scaled particle theory with two different hard sphere diameters for hydrogen-bonded and non-hydrogen-bonded water molecules.[80] The molecular radius of the cavity is calculated using the molecular volume V as $R_{mol} = [3 \cdot V/4 \cdot \pi]^{1/3}$, and the solvent-accessible radius is calculated from $R_{SA} = R_{mol} + \sigma_w/2$, where σ_w is the hard-sphere diameter of water. In the ΔG_d estimates shown below, the molecular volumes of alkanes are calculated using the additivity scheme,[81] and the diameter of water is equal to 0.28 nm in the

(70) Fritz, J.; Katopodis, A. G.; Kolbinger, F.; Anselmetti, D. *Proc. Natl. Acad. Sci. U.S.A.* **1998**, *95*, 12283–12288.
(71) Smith, D. A.; Brockwell, D. J.; Zinober, R. C.; Blake, A. W.; Beddard, G. S.; Olmsted, P. D.; Radford, S. E. *Philos. Trans. R. Soc. London, Ser. A* **2003**, *361*, 713–728.
(72) Sharma, D.; Perisic, O.; Peng, Q.; Cao, Y.; Lam, C.; Lu, H.; Li, H. B. *Proc. Natl. Acad. Sci. U.S.A.* **2007**, *104*, 9278–9283.

(73) Ashbaugh, H. S.; Paulaitis, M. E. *J. Am. Chem. Soc.* **2001**, *123*, 10721–10728.
(74) Southall, N. T.; Dill, K. A. *Biophys. Chem.* **2002**, *101*, 295–307.
(75) Chen, J.; Brooks, C. L., III; Scheraga, H. A. *J. Phys. Chem. B* **2008**, *112*, 242–249.
(76) Miller, T. F.; Vanden-Eijnden, E.; Chandler, D. *Proc. Natl. Acad. Sci. U.S.A.* **2007**, *104*, 14559–14564.
(77) Shimizu, S.; Chan, H. S. *J. Chem. Phys.* **2000**, *113*, 4683–4700.
(78) Hofinger, S.; Zerbetto, F. *Chem. Soc. Rev.* **2005**, *34*, 1012–1020.
(79) Ben-Amotz, D. *J. Chem. Phys.* **2005**, *123*, 184504.
(80) Graziano, G. *Chem. Phys. Lett.* **2006**, *432*, 84–87.
(81) Lepori, L.; Gianni, P. *J. Solution Chem.* **2000**, *29*, 405–447.

cEOS calculations. Figure 8 compares the transition-state free energies for each of the alkane chains estimated from our measurements with the free-energy difference calculated by eq 15 and two cavity models.[79,80] It can be noted that the values are close in range, but the cavity model predicts that ΔG should increase monotonically with increasing alkane size, a trend that is not observed in experimental measurements of $\Delta G^{\ddagger}$.

The surface free energy in these cavity models depends on the solute size. In computer simulations of intermolecular interactions with implicit solvent, the hydrophobic component to the free energy of interactions is usually accounted for by multiplying the excess surface area by the constant surface energy density.[82,83] Although the implicit solvent models oversimplify the hydration phenomena,[77,84–86] their wide use and similarity between measured $\Delta G^{\ddagger}$ and ΔG from cEOS model call for comparison. Two dash-dotted lines in Figure 8 show two dependencies that assume constant surface energy density γ that equals 18 and 31 kJ mol^{-1} nm^{-2}. The latter value corresponds to the water–oil surface tension,[87] and the former was suggested for calculation of the transfer energy of small alkanes from oil to water.[88] The measured values fall between these lines. Using the differences in the solvent accessible areas of separated and collapsed cavities for measured alkanes, we found that an average $\gamma^{\ddagger} = 21 \pm 2$ kJ mol^{-1} nm^{-2} (the double dagger symbol denotes that this surface energy is derived from activation energies). It is interesting to note that this value is much larger than the surface energy of ~ 2 kJ mol^{-1} nm^{-2} that is typically used to account for hydrophobic interactions in computer simulations of proteins and is close to the higher end of the reported range (24 kJ mol^{-1} nm^{-2}).[82] Also, $\gamma^{\ddagger}$ significantly exceeds γ obtained from alkane solubility data (~ 3.8 kJ mol^{-1} nm^{-2}) but is below γ calculated for hexane rotamers (29 kJ mol^{-1} nm^{-2}).[11] By adjusting γ, the implicit solvent model can match the measured $\Delta G^{\ddagger}$ values. However, if the geometry of interacting molecules is preserved, this model predicts an increase in ΔG_{d} with increasing solute size, which is not observed experimentally. This deficiency requires a more complex model.

5.5. Conformations of Alkanes in Monomeric and Dimeric States. The rather close agreement between the measured activation energy and predictions by the cavity models is nonetheless surprising because the cavity model is based on the simple assumption of spherical monomers and dimer and does not use any adjustable parameters. Simulations indicate that the pmf between hydrophobic solutes in water strongly depends on the shape of interacting species.[9] Measurements of solubility[89,90] and theoretical calculations[91,92] indicate that the
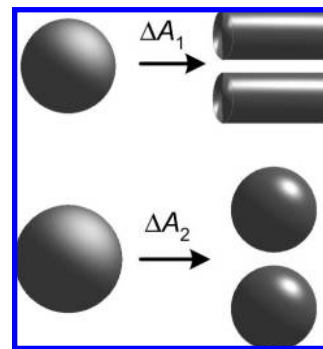

Figure 9. Separation of two alkanes from collapsed state into different conformations. Such separation might occur with similar change in the solvent accessible area $\Delta A_1 \approx \Delta A_2$.

individual alkane molecules of the size used in this study are likely to be in an extended (nonglobular) conformation. However, other studies indicate a possibility of gauche conformations in hydrocarbon chains in water[93–95] with the potential for collapse in molecules longer than hexadecane.[96] Computer simulations predict the collapsed state for longer chains,[96,97] and therefore it is reasonable that the dimers may be in the globular state. Also, experimental measurements of conformational flexibility of alkanes in the liquid state indicate possible deviations of molecular conformations from the all-trans geometry.[98,99] It might be suggested that the nonmonotonic dependence of $\Delta G^{\ddagger}$ on size of alkanes reflects the differences in conformational changes during dissociation for alkanes from dodecane to octadecane. From a simple geometric argument, the change in the solvent accessible area upon merging of two extended conformations into a collapsed globular state is larger than that for merging of two collapsed molecules. Therefore, the free energy of dissociation of a dimer composed of shorter alkanes (extended in the monomeric state) might be similar in value to the free energy of dissociation of two longer alkanes (collapsed in the monomeric state) as schematically illustrated in Figure 9. This figure exaggerates the differences in conformations (as shown $\Delta A_1 > \Delta A_2$) and serves to represent a concept. From the measured size dependence shown in Figure 8, it is evident that the suggested transition from nonglobular to globular monomeric state occurs for alkanes longer that hexadecane. Actual structures are molecularly complex, and elaborate theoretical modeling[76,97,100] is necessary to test the feasibility of this proposed explanation.

The suggestion that conformational transitions in alkane chains occur during separation is supported by two additional pieces of evidence. (1) If the tethered alkanes in the monomeric state and in the dimer were all-trans linear molecules, then separation of two monomers would occur with an approximately linear increase in the free energy (molecules are sliding apart). Consequently, the measured barrier width $x^{\ddagger}$ should be close to the extended length

(82) Elcock, A. H.; Sept, D.; McCammon, J. A. *J. Phys. Chem. B* **2001**, *105*, 1504–1518.
(83) Williams, D. H.; Stephens, E.; O'Brien, D. P.; Zhou, M. *Angew. Chem., Int. Ed.* **2004**, *43*, 6596–6616.
(84) Levy, R. M.; Zhang, L. Y.; Gallicchio, E.; Felts, A. K. *J. Am. Chem. Soc.* **2003**, *125*, 9523–9530.
(85) Hamelberg, D.; Shen, T. Y.; McCammon, J. A. *J. Chem. Phys.* **2006**, *125*, 094905.
(86) Lum, K.; Chandler, D.; Weeks, J. D. *J. Phys. Chem. B* **1999**, *103*, 4570–4577.
(87) Israelachvili, J. N. *Intermolecular and Surface Forces*, 2nd ed.; Academic Press: New York, 1991.
(88) Brem, R.; Chan, H. S.; Dill, K. A. *J. Phys. Chem. B* **2000**, *104*, 7471–7482.
(89) Smith, R.; Tanford, C. *Proc. Natl. Acad. Sci. U.S.A.* **1973**, *70*, 289–293.
(90) Tolls, J.; van Dijk, J.; Verbruggen, E. J. M.; Hermens, J. L. M.; Loeprecht, B.; Schuurmann, G. *J. Phys. Chem. A* **2002**, *106*, 2760–2765.
(91) Wallqvist, A.; Covell, D. G. *Biophys. J.* **1996**, *71*, 600–608.
(92) Mountain, R. D.; Thirumalai, D. *Proc. Natl. Acad. Sci. U.S.A.* **1998**, *95*, 8436–8440.
(93) Hermann, R. B. *Proc. Natl. Acad. Sci. U.S.A.* **1977**, *74*, 4144–4145.
(94) Rosenberg, R. O.; Mikkilineni, R.; Berne, B. J. *J. Am. Chem. Soc.* **1982**, *104*, 7647–7649.
(95) Beglov, D.; Roux, B. *J. Chem. Phys.* **1994**, *100*, 9050–9063.
(96) Mountain, R. D.; Thirumalai, D. *J. Am. Chem. Soc.* **2003**, *125*, 1950–1957.
(97) Athawale, M. V.; Goel, G.; Ghosh, T.; Truskett, T. M.; Garde, S. *Proc. Natl. Acad. Sci. U.S.A.* **2007**, *104*, 733–738.
(98) Goodsaidzalduondo, F.; Engelman, D. M. *Biophys. J.* **1981**, *35*, 587–594.
(99) Holler, F.; Callis, J. B. *J. Phys. Chem.* **1989**, *93*, 2053–2058.
(100) MacCallum, J. L.; Moghaddam, M. S.; Chan, H. S.; Tieleman, D. P. *Proc. Natl. Acad. Sci. U.S.A.* **2007**, *104*, 6206–6210.

of the alkane chains. The extended lengths of alkane chains studied here are in the range from 1.5 to 2.3 nm, but the $x^{\ddagger}$ estimated using the appropriate triangular potential (Bell−Evans) model is in the range from 0.4 to 0.7 nm. Therefore, all-trans conformations in both the monomeric and dimeric states are unlikely. (2) The average barrier width $x^{\ddagger}$ estimated using the two-bond model is 0.60 nm. Simulations of pmf of hydrophobic molecules give $x^{\ddagger}$ in the range from ∼0.15 to ∼0.3 nm.[10,14,15,77,101,102] Our measurements of interactions between large (in comparison to alkanes studied here) but rigid fullerene molecules give $x^{\ddagger}$ of ∼0.35 nm.[33] Simulations of pmf for α-helixes with 20 Ala side chains[100] show $\Delta G^{\ddagger}$ of ∼65 kJ mol^{-1} that is noticeably higher than $\Delta G^{\ddagger}$ measured for alkanes here (∼45 kJ mol^{-1}). However, the $x^{\ddagger}$ predicted for Ala$_{20}$ helixes is considerably lower (∼0.25 nm) than the barrier width $x^{\ddagger}$ obtained for alkanes here.[100] Therefore, large $x^{\ddagger}$ values are consistent with distortion of the dimer conformation before the separation.

The suggested conformational change in alkanes upon dimerization overcomes the tendency of alkane chains to remain in extended conformations and can be compared to the significant conformational transitions in alkane chains that are observed in structures that restrict the end-to-end distance of alkane chains[103] and in binding of surfactant molecules to the synthetic hydrophobic cavities.[104,105] Transition to helical conformations upon binding to cavitand in water is driven by hydrophobicity of 12-carbon alkane chains, although this conformation introduces ∼10 kJ mol^{-1} strain to the chain.[104] Similarly to this binding reaction, the suggested globular state of the alkane dimer decreases the solvent accessible area in the associated state. However, conformational change upon dimerization occurs without limiting geometrical constraints imposed by interacting with the counterpart.

In self-assembly theories of surfactants, the restriction on conformational flexibility of alkane chains contributes unfavorably to the free energy of micellization.[106] This deformation free energy influences the critical micelle concentration and the aggregation number. The collapsed state of the dimer proposed here has implications on the progress of micellar self-assembly: During progress of micellization the collapsed conformation of alkane chains should change into more extended conformations. It is likely that such a transition will initially accelerate the very early steps of self-assembly by releasing the conformational strain in alkanes and then decelerate the assembly by the buildup of the deformation free energy. However, detailed consideration of possible effects is beyond the scope of this article.

6. Conclusions

Pairwise interactions between alkanes from decane to octadecane have been studied by single molecule force spectroscopy.

Alkanes were covalently attached to the glass substrate and AFM probe with hydrophilic PEG tethers. A double-tether approach was employed, and only the force curves with ruptures corresponding to stretching of a polymeric tether with length of twice the single tether length were selected for the subsequent analysis. Rupture force data were analyzed using a common most probable force approach as well as a new model that simultaneously fits the measured distributions of rupture forces with one set of the kinetic parameters, as well as taking into account possible two-bond ruptures. In both data analysis approaches, the possible systematic errors due to tether stiffening and variations in the shape of the potential of mean force were compensated for by using a model that accurately describes stretching of PEG tethers in water and by using two different kinetic models of the forced bond rupture. The standard data analysis approach is insufficient to explain the tail of high forces found in experimental data and gives a large variation in the extracted kinetic parameters measured in separate experiments. The two-bond model accurately describes the distributions of rupture forces measured on different samples using one set of kinetic parameters. This data analysis makes no assumptions regarding the nature of the interactions under study, whether they are nonspecific, as measured here, or specific (such as antibody−antigen interactions, etc.).

The determined activation energies are similar to predictions of two cavity models describing hydrophobicity. The average surface energy density for all alkanes understudy was found to be $\gamma^{\ddagger} = 21 \pm 2$ kJ mol^{-1} nm^{-2}, similar to the microscopic free energy derived from hydrocarbon transfer from oil to water, ∼17 kJ mol^{-1} nm^{-2}. The cavity models predict a monotonic increase in dissociation free energy with size of the hydrocarbon, a feature not found in the measured alkane separation free energies. To explain this discrepancy, it is proposed that the dimers of alkanes studied here and monomeric octadecane are in the collapsed state while shorter monomeric alkanes adopt extended conformations in water. This suggestion is also supported by the measured distances to the activation barrier, which average to 0.60 nm. This barrier width is noticeably larger than the barrier width of ∼0.35 nm measured for dissociation of significantly larger but rigid fullerene C$_{60}$ molecules. This study suggests that conformation changes in alkane chains might occur without imposing strict geometric limitations on alkane chains in the associated state and that the proposed conformational transitions might affect the kinetics of micelle self-assembly.

Supporting Information Available: Descriptions of the data analysis procedures and a description of the extended FJC model. Fits of the discussed statistical models to the rupture force data for all samples studied in this work. This material is available free of charge via the Internet at http://pubs.acs.org.

JA801568Y

(101) Makowski, M.; Liwo, A.; Scheraga, H. A. *J. Phys. Chem. B* **2007**, *111*, 2910–2916.
(102) Pratt, L. R.; Chandler, D. *J. Chem. Phys.* **1977**, *67*, 3683–3704.
(103) Stahl, J.; Bohling, J. C.; Bauer, E. B.; Peters, T. B.; Mohr, W.; Martin-Alvarez, J. M.; Hampel, F.; Gladysz, J. A. *Angew. Chem., Int. Ed.* **2002**, *41*, 1872.
(104) Trembleau, L.; Rebek, J., Jr *Science* **2003**, *301*, 1219–1220.
(105) Purse, B. W.; Rebek, J., Jr. *Proc. Natl. Acad. Sci. U.S.A.* **2006**, *103*, 2530–2534.
(106) Nagarajan, R.; Ruckenstein, E. *Langmuir* **1991**, *7*, 2934–2969.